



# Temperature distribution on anodic surface of membrane electrode assembly in proton exchange membrane fuel cell with interdigitated flow bed



Hang Guo<sup>\*</sup>, Mao Hai Wang, Jia Xing Liu, Zhi Hua Nie, Fang Ye, Chong Fang Ma

MOE Key Laboratory of Enhanced Heat Transfer and Energy Conservation, and Beijing Key Laboratory of Heat Transfer and Energy Conversion, College of Environmental and Energy Engineering, Beijing University of Technology, Beijing 100124, China

## HIGHLIGHTS

- We measure temperature fields on MEA surface in a PEMFC with interdigitated flow field.
- Highest temperature on anodic surface of MEA exists in bottom bordered two side channels.
- Lowest temperature on anode surface of MEA is observed closed to inlet of middle channel.

## ARTICLE INFO

### Article history:

Received 14 June 2014

Received in revised form

18 September 2014

Accepted 25 September 2014

Available online 2 October 2014

### Keywords:

Infrared thermal imaging

Interdigital channel flow bed

Membrane electrode assembly

Proton exchange membrane fuel cells

Temperature distribution

## ABSTRACT

Temperature distribution on the surface of a membrane electrode assembly (MEA) significantly influences the performance, lifetime, and reliability of proton exchange membrane fuel cells (PEMFCs). Entire temperature fields on the surface of an MEA anode side under an interdigitated flow field are experimentally measured at non-humidification conditions with a self-designed PEMFC and infrared imaging technology. The highest temperature on the surface of the MEA anode side appears in the bottom bordered two side channels, and the lowest temperature exists in the area closed to the inlet of the middle channel. The hot region on the surface of the MEA anode side is easy to locate in the infrared temperature image. The reason for the temperature distribution under the interdigitated flow field is analyzed. The temperature of the MEA, the non-uniformity of temperature distribution on the surface of the MEA anode side, and the fuel cell temperature increase with the loaded current density.

© 2014 Elsevier B.V. All rights reserved.

## 1. Introduction

Temperature distribution in fuel cells affects water balance and other dynamics and transport phenomena that depend on temperature [1]. A membrane electrode assembly (MEA) has high efficiency at high operating temperature. The formation of a local hot spot on the MEA surface because of high temperature destroys the electrolyte membrane and even leads to membrane failure because of the dehydration of the membrane. By contrast, low temperature results in water flooding. Thus, maintaining the best operating temperature of fuel cells ensures uniform temperature distribution on the MEA surface and improves the reliability and lifetime of MEAs.

Many methods are used to measure temperature distribution in fuel cells. These tools include thermocouples, micro temperature sensors based on micro electromechanical system (MEMS) fabrication technology, in-fiber Bragg grating (FBG) sensors, and resistance temperature detectors. These tools are inserted into fuel cells to measure temperature. Mench et al. [1] embedded eight micro thermocouples into two sheets of Nafion membrane to measure the temperature distribution of electrolytes in a fuel cell. Only three thermocouples gave a reliable signal output. The diameter of the thermocouple was the same as the thickness of the electrolytes and thus seriously affected the performance of the fuel cell. He et al. [2] placed two thin-film gold thermistors in two Nafion membrane layers to measure temperature. However, the sensors blocked the channel of ion transfer and thus impaired the performance of the fuel cell. Lee et al. [3] used MEMS technology to fabricate a micro sensor, which was inserted into two parylene thin films to measure the interior temperature of a fuel cell. This method accurately measured the interior temperature distribution of the fuel cell, but

<sup>\*</sup> Corresponding author. Tel.: +86 10 67391612x8311; fax: +86 10 67392774.

E-mail addresses: [hangguo@sohu.com](mailto:hangguo@sohu.com), [hangguo@bjut.edu.cn](mailto:hangguo@bjut.edu.cn) (H. Guo).

fabrication was complex. The sensor affected the performance of the fuel cell to some extent. David et al. [4] used an FBG sensor to measure the interior temperature of a fuel cell. Non-conducting fiber has no effect on electromagnetic interference and requires no isolation. Only the mean temperature of the fiber area and not the temperature of a point can be obtained. Inman et al. [5] placed an optic sensor on the ridge of the channel plate of a specially designed fuel cell to measure temperature through the contact of the sensor and gas diffusion layer. Each sensor consisted of phosphor, a fiber-optic light guide, an optic splitter, an excitation source, and a photodetector. Considering that the attenuation coefficient of the sensor decreased with increasing temperature, the method can measure the temperature between the gas diffusion layer and cathode bipolar plates of a fuel cell in situ. The sensor was highly sensitive, but fabrication was complex.

In addition to inaccurate measurement, inserting the sensor into the fuel cell to measure temperature is accompanied by contact resistance and fuel leakage, which change the operating conditions of the fuel cell and impairs its performance. Moreover, measurement technologies associated with high fabrication cost and manufacturing difficulty are complex, sensors are easily damaged in the manufacturing process, the sensitivity and measurement accuracy of sensors cannot meet the demand, and neither the temperature field of the entire channel region or MEA surface nor transient temperature can be obtained. Therefore, non-contact temperature measurement technology without effects on fuel cells is favored by many researchers.

### 1.1. Infrared imaging technology

Infrared imaging is an important technology for measuring temperature distribution. This method is a wavelength transform technology that transforms infrared light radiated by analytes into visible light. Infrared imaging produces two-dimensional images by distinguishing the different parts of thermal radiation. As a non-contact method for measuring temperature, this method does not require the placement of a sensor in the fuel cell and thus effectively eliminates the effects of temperature measurement equipment on the performance of fuel cells. This measurement technology has several other advantages. The internal structure of a fuel cell does not need to be changed, temperature distribution on the entire surface can be obtained, and temperature measurement has a wide range. Real-time temperature distribution on the MEA surface in fuel cells can be accurately measured with an appropriate end plate, which allows infrared light to pass through.

### 1.2. Measuring temperature on outside surface of fuel cell by infrared imaging

Infrared imaging is an effective way to obtain non-uniform heat production and temperature distribution in operating fuel cells and fuel cell stacks. Infrared imaging does not use sensors and barely influences the overall performance of fuel cells. This method is also suitable for measuring temperature on the outside surface of fuel cells. Wang et al. [6] used thermo-tracer TH5102 to measure temperature on the exterior cathode surface of a proton exchange membrane fuel cell (PEMFC). The range of temperature measurement was  $-20^{\circ}\text{C}$ – $800^{\circ}\text{C}$ . The material of the anode end plate and polar plate was copper and graphite, respectively; that of the cathode end plate was organic glass. The cathode was machined with a parallel channel. Temperature distribution on the cathode surface changed with fuel cell temperature and oxygen flow. Shou et al. [7] used a thermal infrared imager with an accuracy of  $0.1^{\circ}\text{C}$  to measure temperature on the cathode surface of a micro PEMFC at different operating conditions. They compared their observation

with the results of numerical computation and thereby demonstrated the applicability of infrared imaging to surface temperature measurement. Scholta et al. [8] designed an external liquid-cooling system to cool a high-temperature PEMFC stack with an operating temperature of  $140^{\circ}\text{C}$ – $180^{\circ}\text{C}$ . They studied temperature distribution on the external surface of the vertical section when the fuel cell stack operated at start-up and steady conditions with infrared imaging.

NASA's Jet Propulsion Laboratory [9] used a thermal infrared imager to investigate temperature distribution of fuel cells and fuel cell stacks. A thermal infrared imager with a temperature detection accuracy of  $0.005^{\circ}\text{C}$  was machined with a high-quality infrared photodetector, which effectively monitored the temperature distribution of the operating fuel cell. Temperature variations on the cathode side of a six-fuel-cell stack at open-circuit and loading conditions were investigated. The non-uniform distribution of fuel on the electrode surface resulted in different current densities and thus generated non-uniform heat. The high crossover rate of methanol in one of the single cells caused temperature distribution on the cathode surface to become higher than that in other single cells. Thermal infrared imaging reliably yields the temperature field on the cathode surface of fuel cell stacks, but it cannot obtain the temperature value of an exact point.

Thermal infrared imaging also effectively measures temperature distribution on the cathode surface of solid oxide fuel cells (SOFCs) on-line. The accuracy of the temperature measurement of a thermal infrared imager depends on the degree of the viewing angle, which is the ratio of the distance between the thermal infrared imager and analyte to the diameter of the facula. Brett et al. [10] used a Cedip silver infrared imager, which is sensitive to wavelengths between 3 and  $12\text{ }\mu\text{m}$ , to measure temperature distribution on the cathode surface of a button SOFC on-line, but the low quality of the image affected the resolution ratio. The distance between the thermal infrared imager and analyte was 0.3 m. The measurement accuracy was  $0.1^{\circ}\text{C}$ , and the spatial resolution was 0.5 mm. Temperature variation with different current densities was obtained. Ju et al. [11] used infrared imager ThermoCAM SC100, which is sensitive to wavelengths between 3 and  $12\text{ }\mu\text{m}$ , to investigate the response of transient temperature on the cathode surface of an SOFC to current density. The sensitivity of the infrared imager was  $0.1^{\circ}\text{C}$ . Infrared imaging provided a non-destructive method for measuring temperature on the surface of an operating SOFC by numerical simulation. Furthermore, Du et al. [12] studied the thermal image of a micro tubular SOFC at cold and hot ambient surroundings with a thermal infrared camera. The given image was not detailed, and the thermal image of the fuel cell at open-circuit voltage and loading conditions was not given. Guo et al. [13,14] used thermal infrared imager OMEGA OS 3707 to measure the surface temperature of a button SOFC with a diameter of about 2 mm. Because of the small size of the fuel cell, a Sagnac optic device was used to allow some light (300 nm–1000 nm) to spread to the thermal infrared imager to update the viewing angle. Lawlor et al. [15] measured the temperature of a micro tubular SOFC in a high-temperature wind tunnel with an infrared imager. A black line represented the low temperature in the temperature chart because infrared light could not radiate to the back of the fuel cell. Thermal infrared imaging produces a detailed profile distribution of the temperature of the whole fuel cell and avoids the poisoning of the cell cathode by the sensor. Therefore, observing the exterior temperature gradient of a fuel cell is an effective approach. Pomfret et al. [16] measured temperature distribution on the anode surface of an operating SOFC with an infrared imaging system similar to a Si charge-coupled device imaging machine, which has a spatial resolution of 0.1 mm and a temperature measurement accuracy of  $0.1^{\circ}\text{C}$ .

Because of the special structure of fuel cells, infrared imaging with high resolution and short response time is suitable for measuring temperature on their outside surface. Infrared imaging captures the temperature fields of the entire measurement area without inserting a sensor into fuel cells and thus has no effect on the overall performance of the cells.

### 1.3. Measuring temperature on MEA surface by infrared imaging

MEA temperature management is one key problem that should be solved to commercialize fuel cells. Embedding a thermocouple or sensor to measure the temperature of the electrolyte membrane of an operating fuel cell cannot obtain detailed temperature distribution. If the number of embedded sensors is insufficient, the hot spot on the electrolyte membrane cannot be located. Local temperature on the MEA surface that exceeds its limit impairs the performance of MEA and even results in MEA failure. Therefore, non-contact infrared imaging becomes the key method of temperature measurement on the MEA surface.

Shimoi et al. [17] demonstrated that the difference in temperature between the carbon electrode surface and electrolyte membrane was insignificant by one-dimensional heat conduction calculation. They suggested that the small difference in temperature can be neglected. Thus, the temperature on the carbon electrode surface equaled the temperature of the electrolyte membrane. Three parallel channels (100 mm long, 3 mm wide, and 1 mm deep) were made on the anode and cathode channel plates of the fuel cell to form an active area of 18 cm<sup>2</sup>. The cathode of the fuel cell was specially designed, and parts of the cathode plate used sapphire as the measurement window for the infrared imager. The authors investigated the temperature on the carbon electrode surface at the cathode side of an operating PEMFC with infrared imager TH5104. The infrared imager, which had a measurement accuracy of 2 °C–3 °C, was sensitive to wavelengths between 3.0 and 5.3 μm. Only the temperature distribution of the middle channel region, not of the entire channel region, was obtained because water was generated in two channels. Experimental results indicated that the temperature of the electrolyte membrane increased with current density, and condensate water emerged on the sapphire plate where infrared light passed through, and increased temperature on the channel outlet. However, this temperature was not the true temperature of the membrane. Therefore, the measurement of temperature on the carbon electrode surface as the temperature on the MEA surface is inaccurate.

Hakenjos et al. [18,19] remade the cathode side of a PEMFC. Zinc selenide, which enables infrared light to pass through, was used to seal the gas channel and to allow a direct view onto the gas diffusion layer. The authors measured temperature distribution on the active area on the cathode side of the fuel cell. The infrared imager was sensitive to infrared wavelengths between 8 and 12 μm with an error of 0.3 °C at 30 and 60 °C. Because liquid water accumulated on the surface of the zinc selenide window, only temperature distribution on the area without liquid water, not the entire channel, was obtained. Experimental results indicated that temperature was only a function of current density on the area without liquid water. Moreover, because the zinc selenide window enables visible light to pass through, water droplet condensation on the cathode gas channel of the fuel cell can be observed.

To prevent the liquid water generated on the cathode side from resulting in an inaccurate description of the temperature distribution on the MEA surface, Wang et al. [20] measured temperature distribution on the MEA surface at the anode side of a specially designed PEMFC with infrared imaging technology. Barium fluoride was used as an anode transparent window for the infrared light of the tested fuel cell; this material enables the direct observation of

MEA through anode serpentine channels. The authors used thermo tracer TH5102, which is sensitive to infrared lengths between 8 and 12 μm, to describe temperature distribution on the MEA surface of the entire serpentine channel region and thereby accurately located the hot spot on the MEA surface. The average temperature on the MEA surface and the temperature of the fuel cell increased with current density. High current density worsened the non-uniformity of temperature distribution on the MEA surface. The temperature gradient between the gas inlet and outlet was 5 °C at high current density. Knowledge of temperature distribution on the MEA surface of the entire channel region enables reasonable heat management and enhances fuel cell design. Previous researchers have used infrared imaging to measure temperature distribution inside a fuel cell, but they obtained only the local temperature distribution of a region without liquid water. By contrast, Wang et al. obtained temperature distribution on the MEA surface of the entire channel region. This distribution facilitates the description of the thermal behavior of fuel cells and the location of the local hot spot on the MEA surface. In a previous study [21], we used infrared imaging technology to measure temperature distribution on the MEA surface of the entire parallel channel region. However, this measurement method was limited. Dry reactants were supplied as fuel to avoid the effect of liquid water on the accuracy of temperature measurement; this effect limited the best performance of the fuel cell.

Hot spots cause the thermal decomposition of electrolyte membranes. Thus, temperature distribution in fuel cells should be obtained. Non-contact on-line temperature measurement effectively measures temperature distribution in fuel cells. Nishimura et al. [22,23] used an infrared imager to measure temperature distribution on the cathode serpentine channel of a specially designed PEMFC; the measured temperature distribution inside the PEMFC was 343 K–353 K. The cathode end plate, collector plate, and hot water passage plate of the PEMFC were drilled to form an observation window. This method can accurately measure temperature distribution on the cathode gas diffusion layer. Infrared imager TH9100WL, which has a spatial resolution of 1.2 mm and an accuracy of 0.1 °C, was used to investigate the effect of the gap between gas channels on temperature distribution. The observation window only slightly affected the energy output of the fuel cell. The performance of the test fuel cell with an observation window decreased by about 7% as current density was 0.8 A cm<sup>-2</sup>. The effect of the gap between gas channels on temperature was also tested. The temperature of the observation region decreased with the decreasing gap between gas channels. A small gap between gas channels made gas, water, and temperature distribution on the reaction surface uniform and thus improved the performance of the fuel cell. This measurement method avoided the effect of gas fuel leakage because of the inadequate bonding pressure of the transparent glass window and liquid water on the performance of the fuel cell and on the accuracy of temperature measurement. To avoid gas leakage and the deterioration of fuel cell performance, a separator was installed between the gas channel and diffusion layer. Temperature distribution on the back of the separator and not that on the electrochemical reaction interface between the cathode electrolyte membrane and the catalyst layer of the fuel cell was obtained.

Infrared imaging achieves several objectives, including obtaining the temperature distribution of the entire channel region inside a fuel cell, accurately locating the hot spot on the MEA surface, and providing direction on the heat management and optimal design of fuel cells. This method has no effect on the overall performance of fuel cells because an embedded sensor is not required. By contrast, using infrared imaging to measure the temperature distribution of MEA inside a fuel cell has limitations, such as the requirements of

changing the structure of the fuel cell, using special material for infrared light to pass through as the plate of the fuel cell, and avoiding the generation of liquid water during testing. Therefore, infrared imaging technology is suitable only for measuring the temperature of single cells or the end plate of a fuel cell stack. Obtaining temperature on either the flow field plate outside the surface or the end plate cannot accurately evaluate the temperature on the MEA surface.

#### 1.4. Other non-contact technologies for measuring temperature

Basu et al. [24] used the tunable-diode laser absorption spectrum method for the non-contact on-line measurement of the partial pressure and temperature distribution of vapor in a serpentine gas channel at the cathode side of a PEMFC. The measurement technology was based on the sensitivity of the absorption characteristic of water to a certain range of temperature and partial pressure. The accuracy of temperature measurement was 2 °C between 60 and 85 °C. A specially designed bipolar plate channel enabled the transfer of diode laser beams along the length direction of the channel. Substance distribution in the bipolar plate channel was uneven when the current changed to steady state and sinusoidal conditions, and the load increase created a large difference in water content between the inlet and outlet. As temperature on the outside surface of the channel was measured, the temperature between the two channels had no systemic variation at the steady state of the operating fuel cell. When the dynamic load change achieved sinusoidal conditions, the temperature of the fuel cell could not reach the equilibrium value. The technology produced superior instant definition. However, it cannot accurately measure temperature when liquid water emerged in the channel, as well as the temperature of an exact position. Only the mean temperature of the entire region can be measured.

When the electrochemical impedance spectrographic method is used to detect the temperature distribution of a fuel cell, the obtained temperature is the center temperature of the fuel cell, and the temperature distribution of one single cell in the fuel cell stack can be determined. Hashimoto et al. [25] used the same method to measure the ohmic drop of a micro tubular SOFC at different operating conditions. The authors evaluated the temperature of the fuel cell by using the linear relation between temperature and resistance and suggested that the temperature of the fuel cell increased with current density. They compared the evaluated temperature with the temperature measured by the thermocouple, which was located 2 mm away from the cathode plate of the fuel cell. This result demonstrated that the method effectively manages the temperature of tubular SOFCs. However, because the thermocouple had no contact with the cathode polar plate of the fuel cell, the measured temperature was not the temperature of the polar plate of the fuel cell. Thus, the data obtained by this measurement method did not agree with the simulation result. Lawlor et al. placed a thermocouple on the cathode polar plate surface of a fuel cell. The authors measured ohmage at open-circuit voltage or approximate open-circuit conditions when the fuel cell generated little heat. This measurement provided data for their calibration. They obtained the temperature of the micro tubular SOFC in a high-temperature wind tunnel through the relation between ohmage and temperature [13].

Temperature distribution inside the fuel cell cannot be effectively and accurately obtained with a laser-induced thermometer. Measurement accuracy depends on the size of the measurement point: a smaller measurement point makes the measurement more accurate [13]. Because the instrument's facula was larger than the tested SOFC diameter, the measured temperature that included the temperature of the cooler on the back of the fuel cell was lower

than the actual temperature of the fuel cell. Although the stability of this temperature measurement device cannot be ensured when a small target is measured, the device effectively measures the temperature of large devices after calibration. In addition, given that micro fuel cells are the next-generation power supply for portable electronic equipment [26], non-contact temperature measurement should be suitable for fuel cells, which tend to be increasingly miniaturized.

Thermal infrared imaging with high spatial resolution and collection frame frequency can function independently of the fuel cell to measure the temperature distribution of the entire channel region inside the cell and the temperature of the outside surface of the cell without a sensor and a connection line. This temperature measurement method can obtain the temperature distribution on the MEA surface inside a fuel cell and locate the local hot spot in a specially designed fuel cell. The tested fuel cell is not polluted or damaged during measurement. However, this method has limited application. The structure of the fuel cell should be altered when measuring the temperature inside it, and a special material transparent for infrared light should be used as the end plate of the cell. This method is unsuitable for measuring the temperature inside a fuel cell stack. The emergence of liquid water on the cathode of a fuel cell affects measurement accuracy. The temperature distribution of the entire region inside the fuel cell cannot be obtained. Therefore, this method is suitable for temperature measurement on the outside surface of a fuel cell and the interior temperature measurement of specially designed single fuel cells or the end plates of fuel cell stacks.

Other non-contact temperature measurement methods expand the research idea of temperature measurement in fuel cells, but these methods have their limitations. For example, the fuel cell requires remanufacture, or only local-region temperature distribution on the outside surface of the fuel cell can be obtained. Therefore, these non-contact methods should be improved for dynamic temperature measurement inside a fuel cell.

The interdigitated flow field has been widely used in PEMFCs since Nguyen [27] firstly proposed this flow field design. It has been reported that the interdigitated flow field showed enhanced transport capabilities [28], which increases the reactant supply to the reactive sites and the cell flooding tolerance. Therefore, the interdigitated flow field shows better performance compared to conventional parallel flow field [28–30] and serpentine flow field [31,32]. The operation conditions such as humidification and fuel cell temperature influence the performance of PEMFCs with interdigitated flow field [28,33]. Knowledge of the temperature distribution in PEMFCs with interdigitated flow field would be helpful for understanding of the optimal flow field design to improve the performance of PEMFCs. Researchers have obtained the temperature distribution in PEMFCs with flow fields such as serpentine or parallel by infrared imaging technology. To the best of our knowledge, applying infrared imaging technology to measure temperature distribution in PEMFCs with interdigitated flow field has not been found in the literature. This study presents a self-designed PEMFC with interdigitated channels to measure temperature distribution on the MEA surface in the entire channel region under different operating conditions with infrared imaging technology and to explore the reason behind temperature maldistribution.

## 2. Experimental

Fig. 1 shows the structure of the test fuel cell. Interdigitated channels (3 mm channel width, 1.5 mm rib width, and 2.5 mm channel depth) were machined through stainless steel plates to form an active area of 29 mm × 39 mm. Both the anode and the cathode were interdigitated flow fields. Anode channels were



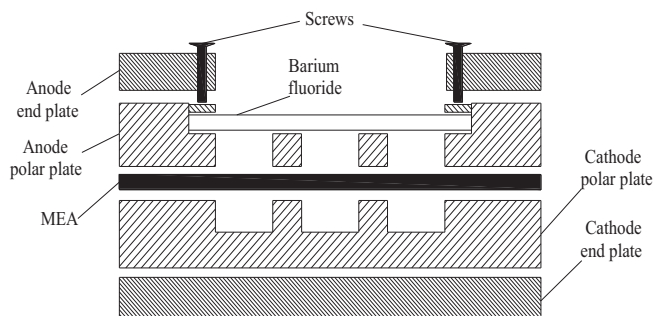


Fig. 1. Structure of experimental PEMFC.

completely broken through to allow a straight view onto the anode surface of the MEA. The anode rather than the cathode side of the MEA was used as the measuring surface because the liquid water that would emerge at the cathode side would result in an inaccurate description of temperature distribution over the MEA surface [17,19]. Gold was coated over the plates as corrosion protection. The anode gas channels were covered by barium fluoride. Because barium fluoride is transparent for infrared light, the anode temperature distribution of the MEA could be observed with an infrared thermo-tracer (NEC, TH5102), which is sensitive to infrared wavelengths between 8 and 12  $\mu\text{m}$ . A catalyst ( $\text{Pt C}^{-1}$ ,  $0.8 \text{ mg cm}^{-2}$ ) was applied onto the gas diffusion layers (carbon paper) with Nafion<sup>TM</sup> solution. The thickness of the gas diffusion layer was 0.3 mm. The electrodes were hot-bonded with a Nafion<sup>TM</sup> membrane (89  $\mu\text{m}$  thick) to form a single sheet.

To obtain accurate temperature readings, the actual emissivity of the measured surface of the MEA should be identified. A black body (the window protective cap of the thermo-tracer) and the MEA were maintained at the same temperature. The thermo-tracer was used to obtain the temperature of the black body by setting emissivity to 1.0. The temperatures of the MEA surface were then measured with the thermo-tracer at various emissivities. The emissivity at which the temperature on the MEA surface was equal to that of the black body was considered the emissivity of the MEA surface. The emissivity of the surface was set to 0.96 with the method presented above.

The transmission of the thermo-tracer was measured with a Fourier spectrometer (BRUKER, EQUINOX55). Fig. 2 shows the

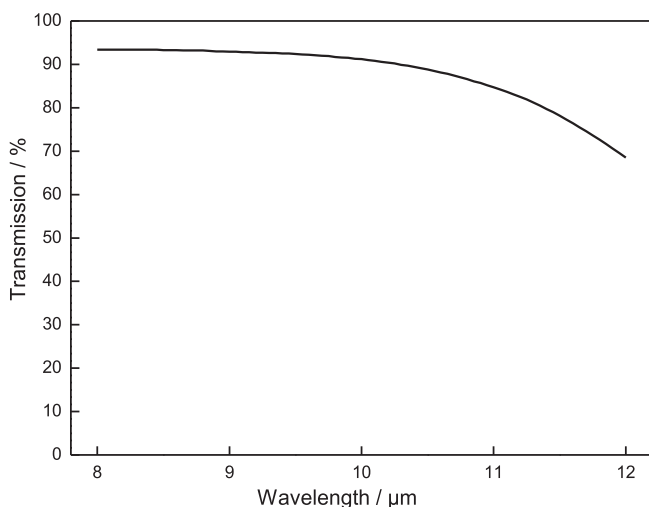


Fig. 2. Fourier spectrogram of barium fluoride window between 8 and 12  $\mu\text{m}$  wavelength.

transmission over the sensitive infrared wavelength. The average transmission was 87.8%, which was sufficient for the material to act as an infrared window.

Both the precision of the thermo-tracer and the absorption of the barium fluoride caused a measurement error. A calibration was conducted to overcome the problem. The real temperatures measured with a copper–constantan thermocouple (the copper and constantan wires had a diameter of 0.5 mm) were compared with the temperatures captured by the thermo-tracer behind the barium fluoride when emissivity was 0.96. A correlation between the two sets of temperature was obtained. The result shown in Fig. 3 implies a correctional equation (Eq. (1)), which was used to convert the data in Figs. 8 and 9.

$$T = 1.066T_{\text{IR}} - 0.971 \quad (1)$$

Mass flow controllers were used to control the flow rates of hydrogen and oxygen. Non-preheated hydrogen and oxygen were supplied in our experiment. The flow rates of hydrogen and oxygen were 300 and 500  $\text{ml min}^{-1}$ , respectively. The gases were supplied in a co-flow direction. A temperature and heating control unit was used to heat the cell and control cell temperature. An electrical load device (ARBIN FCTS LNR) was used to supply the required change in electric load. Atmospheric temperature was 15  $^{\circ}\text{C}$ .

A T-type thermocouple was inserted into the middle of the cathode flow field plate to monitor temperature, which was taken as the fuel cell temperature in this study. A heating pad was installed behind the cathode flow field plate to preheat the plate to an initial temperature. The initial temperature before the loading current was called the preheated fuel cell temperature, which was controlled at 25  $^{\circ}\text{C}$ .

### 3. Results and discussion

Fig. 4 shows the polarization curve of the tested fuel cell. The polarization curve is obtained at a certain operation condition as can be seen in Fig. 4. The flow rates of oxygen and hydrogen are 300  $\text{ml min}^{-1}$ . Although the anode of the fuel cell is specially designed, performance remains high and thus ensures the accuracy of the measurement of the temperature distribution.

Fig. 5 shows the typical temperature distribution on the surface of the MEA anode side of the tested fuel cell. Fig. 5(a) shows the measured temperature distribution, and Fig. 5(b) shows the revised result according to Eq. (1). The inlet of the interdigitated flow field

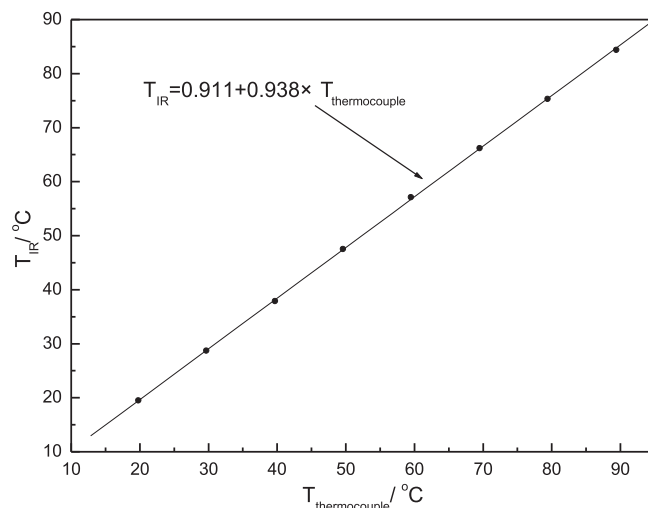


Fig. 3. Correlation of temperature measured with thermo-tracer and thermocouple.

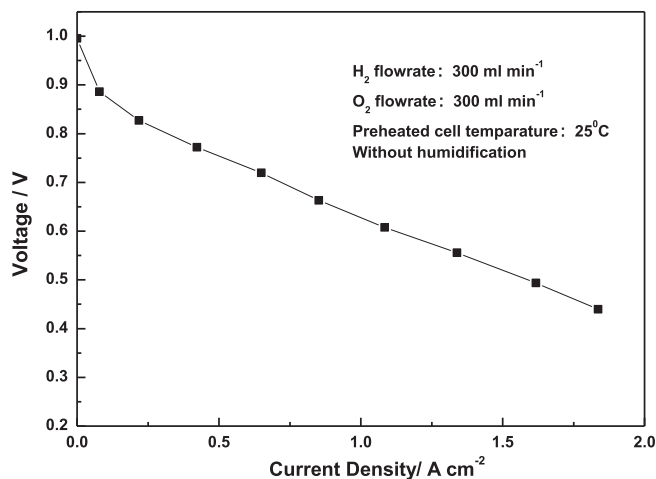
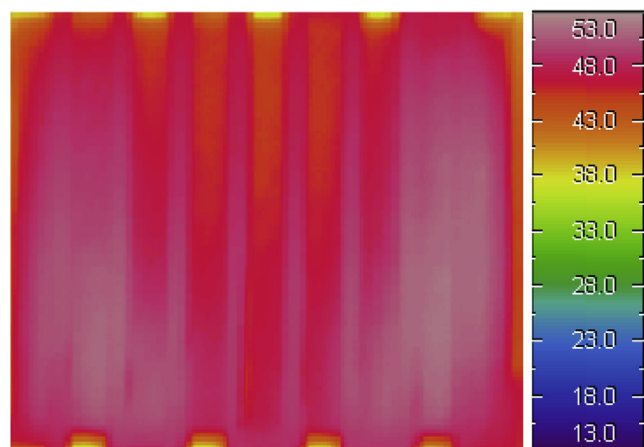
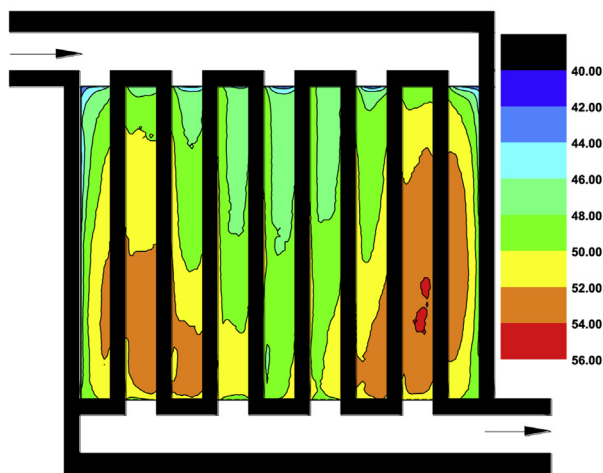


Fig. 4. Polarization curve of test fuel cell.

is located in the upper left corner, and the outlet is found in the lower right corner. The temperature field is captured 3600 s after a current density of  $1.379 \text{ A cm}^{-2}$  is loaded. Fig. 5 shows that the high-temperature region appears in two side channels and the low-



(a) Measurement result



(b) Conversion result

Fig. 5. Typical temperature distribution on surface of MEA anode side of fuel cell.

temperature region appears in the middle channels under the interdigitated channels. The inlet channels of the interdigitated flow field are parallel channels. The flow rate in the middle channels is low, and those in the two side channels are high under parallel channels. This phenomenon has been approved by many studies [34–37]. Besides, one can find evidence that the flow rate in the middle channels is lower than that in the two side channels under interdigitated flow field [38]. In the interdigitated flow channels, gases are forced from the inlet channels into the diffusion layer before reacting at the catalyst layer and finally coming out of the outlet channels. Thus, the gases require a high flow rate to come out of the outlet channels. Because the high flow rates at the two side channels of the interdigitated channels make the flow process smooth, the electrochemical reaction becomes sufficient and increases the current density to form a high-temperature region. By contrast, the middle channels form a partial low-temperature region because of the low flow rate. The hot spot on the surface of the MEA anode side can easily be located in Fig. 5. Compared with that in serpentine [20] or parallel [21] flow field, the hot spot varies and the temperature distribution is quite different. All the temperature distributions in these three flow fields are nonuniform, which are mainly caused by the flow distribution. It indicates that the flow fields should be optimized to obtain a uniform flow distribution and thus ensures a more uniform temperature distribution in fuel cells.

Fig. 6 shows the images of the temperature fields on the surface of the MEA anode side at different current densities. Each picture is taken 60 s after the loading current. The flow rates of hydrogen and oxygen are 300 and 500  $\text{ml min}^{-1}$ , respectively. The temperature of the MEA surface increases with the loaded current density because heat generation increases with the current density of the fuel cell [1]. Temperature on the surface of the MEA anode side increases with flow direction in each channel. The temperature of the gases that enter into each channel is lower than that on the surface of the MEA anode side. Thus, the transfer of convective heat between the reactants and the surface of the MEA anode side reduces the inlet temperature of each channel. In addition, because dry reactants are supplied in the experiments, all the water needed in the membrane and the anode comes from the cathode product of the electrochemical reaction. Membrane hydration is low at the beginning, when gases enter the channel. Along the flow direction in each channel, water is increasingly produced in the channel as the electrochemical reaction progresses. Membrane hydration increases, and more liquid water diffuses back to the anode. Therefore, local current density increases along the flow direction in each channel and thus increases temperature on the surface of the MEA anode side along the same direction. Note that the temperatures at the outlet header of each outlet channel decrease. Although the membrane hydration increases along the flow direction and is highest at the outlet region, the accumulated liquid water at this region will weaken the mass transport, and thus leading to a decrease of temperature in this region.

To compare the temperature fields under different operating conditions in a chart, the temperatures at 27 points in the flow field (Fig. 7) are taken from visualized temperature fields and are converted through Eq. (1). Fig. 7 also shows the active temperature distribution area ( $39 \text{ mm} \times 29 \text{ mm}$ ), which is transparent for infrared light. The inlet of the interdigitated flow field has five channels, and the outlet has four channels.

Fig. 8 shows the effect of the loaded current density on the temperature field on the surface of the MEA anode side. Data are obtained from the images in Fig. 6. Both the temperatures and the non-uniformity of temperature distribution on the surface of the MEA anode side increase with the loaded current density. At low current density, given that the needed fuel and oxidants are

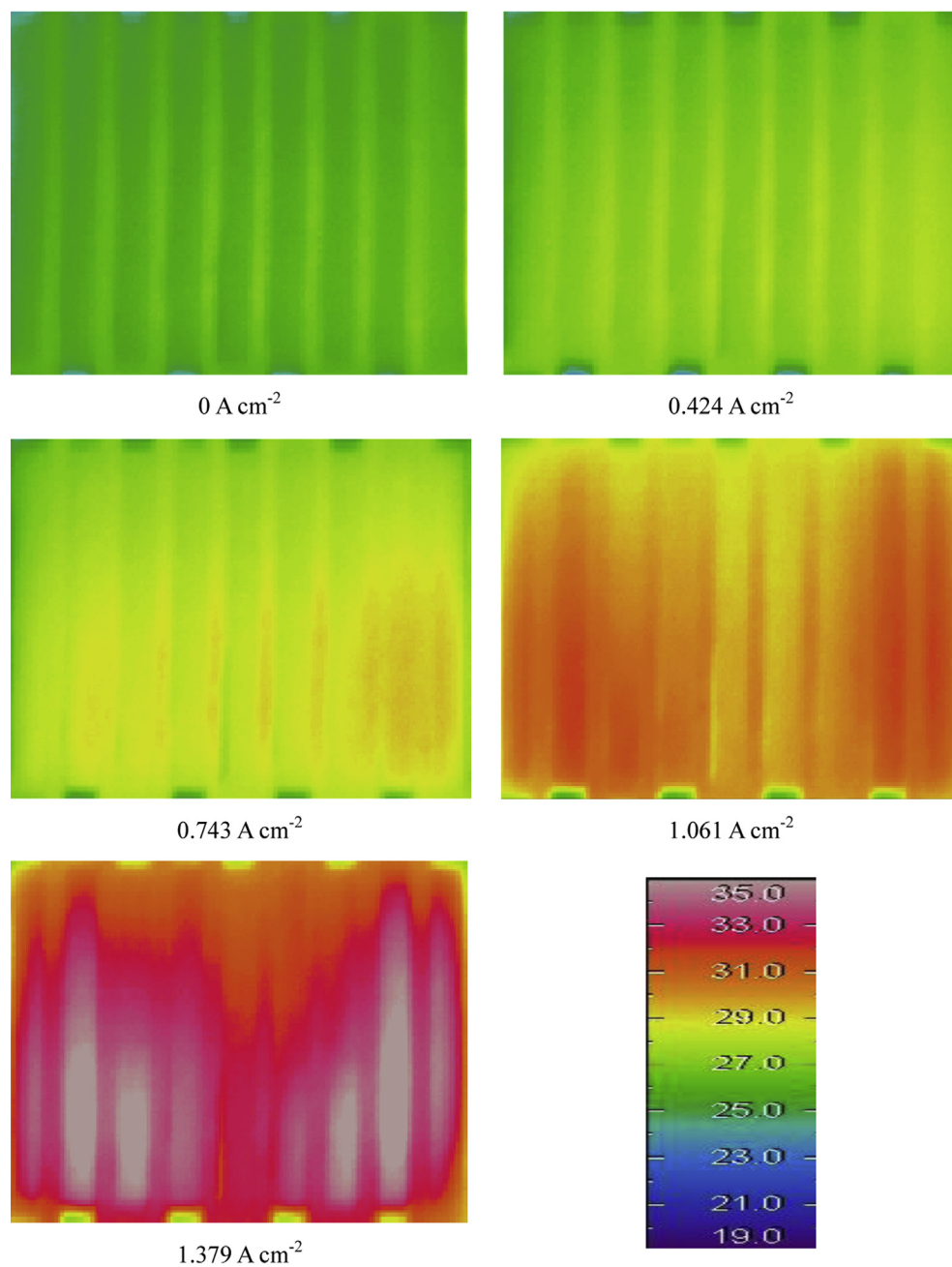


Fig. 6. Temperature fields on surface of MEA anode side at different current densities.

minimal, the reactants supplied in each channel are sufficient. Although the flow rates in the middle channels are low, the electrochemical reaction process continues, and the remaining reactants and products are effectively removed through outlet channels. Increasing current density increases the quantity of reactants, indicating that the gases in the inlet channels require an adequately high flow rate to transport reactants to an active area and to remove residual reactants and products. Two side channels of the interdigitated channels benefit mass transfer because of the high flow rate. The local current density of the two side areas also increases, and much liquid water is generated because of the increased local current density, thereby enhancing the proton conductivity of the membrane covered by the two side channels. As a result, temperature distribution on the surface of the MEA anode

side is not uniform, and this non-uniformity worsens with increasing current density. At high current density, the temperature on the MEA surface at the second and eighth channels counted from left to right is the highest. Moreover, several reactants in the third and seventh channels come out through the second and eighth channels, and all reactants in the first and ninth channels come out through the same channels, which barely happens in other channels. Therefore, the mass transfer in the second and eighth channels is the most massive, and membrane hydration is higher, leading to the highest local current density and temperature of the region.

To better understand the relation between temperature and current density in our case, the highest, lowest and mean temperatures on the MEA surface as a function of current density are

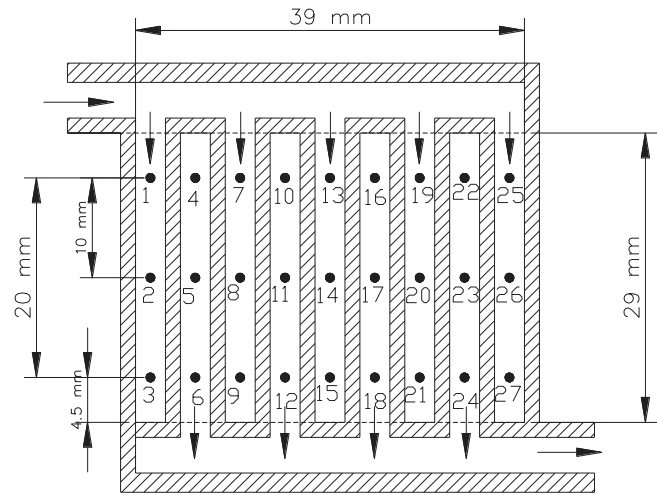


Fig. 7. Positions of temperature points taken from visualized temperature field.

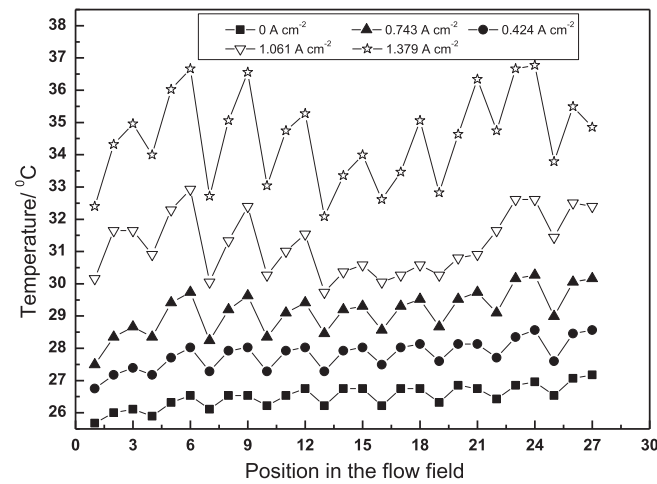


Fig. 8. Effects of current density on temperature distribution on surface of MEA anode side.

plotted in Fig. 9. Given that the temperature is a second order polynomial of the current density [39], polynomial fitting curve is chosen and plotted as solid line in Fig. 9. The statistical data for these polynomial fitting curves are presented in Table 1. As can be

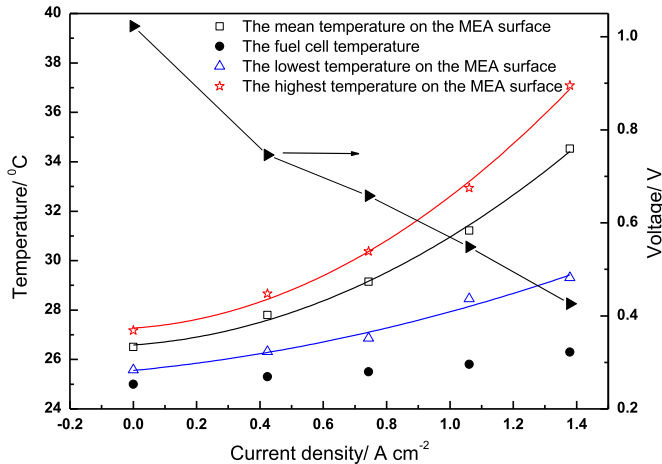


Fig. 9. Variations of MEA temperature and fuel cell temperature with current density.

Table 1  
Statistical data for the polynomial fitting curves in Fig. 9.

	Mean temperature	The highest temperature	The lowest temperature
$A(^{\circ}\text{C})$	26.58699	27.26965	25.55486
$B(^{\circ}\text{C}(\text{A cm}^{-2})^{-1})$	0.89742	0.8557	1.24479
$C(^{\circ}\text{C}(\text{A cm}^{-2})^{-2})$	3.46645	4.46815	1.12904
$r^2$	0.99423	0.99478	0.96411

seen, the polynomial curves fit the temperatures very well and these polynomial fitting curves are second order polynomial in the form of following equation.

$$T = A + B \cdot j + C \cdot j^2 \tag{2}$$

where  $T$  represents temperature,  $j$  is the current density,  $A, B, C$  are coefficients. Therefore, the temperature is a second order polynomial of the current density in our case, which is similar to that in Ref. [39]. Fig. 9 also shows that the lowest and highest temperatures on the surface of the MEA anode side increase with current density. However, the lowest temperature increases more slowly than the highest temperature and thus increases the maximum temperature difference with the current density. Compared with the fuel cell temperature, the MEA temperature increases quickly. The change rules of the temperatures are similar to those in the serpentine channel. The analyses are presented in our previous publication [20]. The performance as shown in Fig. 9 is different with that in Fig. 4 because the flow rates of hydrogen and oxygen are different. This indicates that the flow rates of hydrogen and oxygen affect the cell performance, which may influences the temperature distribution.

Identifying the temperature distribution on the surface of the MEA anode side under an interdigitated flow field facilitates the appropriate heat management of fuel cells with an interdigitated flow field. The non-uniformity of temperature distribution on the surface of the MEA anode side reveals that the flow field needs to be optimized. Thus, mass transport and heat transfer in fuel cells should be investigated to better understand temperature distribution in fuel cells.

4. Conclusions

The entire temperature distributions on the surface of the MEA anode side under an interdigitated flow field are achieved by experiment under the operating conditions described in this study with the self-designed PEMFC and infrared imaging technology. The highest temperature on the surface of the MEA anode side appears at the bottom bordered the two side channels, and the lowest temperature is found in area closed to the inlet of the middle channel. Temperature distribution on the surface of the MEA anode side under an interdigitated flow field is non-uniform. The non-uniformity of flow distribution is one key factor that causes the non-uniformity of temperature distribution under the interdigitated flow field. The temperature and the non-uniformity of temperature distribution on the surface of the MEA anode side under an interdigitated channel increase with the loaded current density. To improve the uniformity of temperature distribution in fuel cells, heat transfer, mass transport, and flow field design should be further investigated.

Acknowledgments

The authors are grateful to the National Natural Science Foundation of China (Grant No.: 51476003), Program for New Century Excellent Talents in University (Grant No.: NCET-10-0006) and



Specialized Research Fund for the Doctoral program of Higher Education (Grant No.: 20121103110009) for the financial support.

## References

- [1] M.M. Mench, D.J. Burford, T.W. Davis, Proceedings of ASME International Mechanical Engineering Congress & Exposition, Washington D.C, 2003, pp. 415–428.
- [2] S. He, M.M. Mench, S. Tadigadapa, Sens. Actuators A 125 (2006) 170–177.
- [3] C.Y. Lee, W.J. Hsieh, G.W. Wu, J. Power Sources 181 (2008) 237–243.
- [4] N.A. David, P.M. Wild, J.W. Hu, N. Djilali, J. Power Sources 192 (2009) 376–380.
- [5] K. Inman, X. Wang, B. Sangeorzan, J. Power Sources 195 (2010) 4753–4757.
- [6] M.H. Wang, H. Guo, C.F. Ma, X. Liu, J. Yu, C.Y. Wang, Chin. J. Power Sources 28 (2004) 764–766.
- [7] S.H. Shou, M.C. Kuan, J. Power Sources 173 (2007) 222–232.
- [8] J. Scholta, M. Messerschmidt, L. Jörissen, C. Hartnig, J. Power Sources 190 (2009) 83–85.
- [9] NASA's Jet Propulsion Pasadena, California, Thermal imaging for Diagnosing Fuel Cells, [http://www.techbriefs.com/index.php?option=com\\_staticxt&staticfile=/Briefs/Nov01/NPO21177.html](http://www.techbriefs.com/index.php?option=com_staticxt&staticfile=/Briefs/Nov01/NPO21177.html).
- [10] D.J.L. Brett, P. Aguiar, R. Clague, A.J. Marquis, S. Schöttl, R. Simpson, N.P. Brandon, J. Power Sources 166 (2007) 112–119.
- [11] G. Ju, K. Reifsnider, X. Huang, J. Fuel Cell Sci. Technol. 5 (2008) 031006.1–031006.6.
- [12] Y. Du, C. Finnerty, J. Jiang, J. Electrochem. Soc. 155 (2008) B972–B977.
- [13] H. Guo, G. Iqbal, B.S. Kang, Proceedings of ASME 2009 Seventh International Fuel Cell Science, Engineering and Technology Conference, Newport Beach, California, 2009, pp. 533–538.
- [14] H. Guo, G. Iqbal, B.S. Kang, Int. J. Appl. Ceram. Technol. 7 (2010) 55–62.
- [15] V. Lawlor, G. Zauner, C. Hochenauer, A. Mariani, S. Griesser, J.G. Carton, K. Klein, S. Kuehn, A.G. Olabi, S. Cordiner, D. Meissner, G. Buchinger, J. Fuel Cell Sci. Technol. 7 (2010) 061016-1–061016-7.
- [16] M.B. Pomfret, D.A. Steinhurst, D.A. Kidwell, J.C. Owrutsky, J. Power Sources 195 (2010) 257–262.
- [17] R. Shimoi, M. Masuda, K. Fushinobu, Y. Kozawa, K. Okazaki, J. Energy Resour. Technol. 124 (2004) 258–261.
- [18] A. Hakenjos, C. Hebling, J. Power Sources 145 (2005) 307–311.
- [19] A. Hakenjos, H. Muentner, U. Wittstadt, C. Hebling, J. Power Sources 131 (2004) 213–216.
- [20] M.H. Wang, H. Guo, C.F. Ma, J. Power Sources 157 (2006) 181–187.
- [21] H. Guo, M.H. Wang, F. Ye, C.F. Ma, Int. J. Hydrogen Energy 37 (2012) 13155–13160.
- [22] A. Nishimura, K. Shibuya, M. Takeuchi, M. Hirota, S. Kato, Y. Nakamura, H. Tachi, M. Narita, J. Therm. Sci. Technol. 4 (2009) 438–452.
- [23] A. Nishimura, K. Shibuya, A. Morimoto, S. Tanaka, M. Hirota, Y. Nakamura, M. Kojima, M. Narita, J. Therm. Sci. Technol. 5 (2010) 319–341.
- [24] S. Basu, M.W. Renfro, B.M. Cetegen, J. Power Sources 162 (2006) 286–293.
- [25] S. Hashimoto, H. Nishino, Y. Liu, K. Asano, M. Mori, Y. Funahashi, Y. Fujishiro, J. Power Sources 181 (2008) 244–250.
- [26] X.H. Wu, H. Guo, F. Ye, C.F. Ma, Prog. Chem. 21 (2006) 1344–1348 (in Chinese).
- [27] T.V. Nguyen, J. Electrochem. Soc. 143 (1996) L103–L105.
- [28] D.L. Wood, J.S. Yi, T.V. Nguyen, Electrochim. Acta 43 (1998) 3795–3809.
- [29] A. Kazim, H.T. Liu, P. Forges, J. Appl. Electrochem. 29 (1999) 1409–1416.
- [30] G. Hu, J. Fan, S. Chen, Y. Liu, K. Cen, J. Power Sources 136 (2004) 1–9.
- [31] A. de Souza, E.R. Gonzalez, J. Solid State Electrochem. 7 (2003) 651–657.
- [32] S.S. Hsieh, S.H. Yang, J.K. Kuo, C.F. Huang, H.H. Tsai, Energy Convers. Manage. 47 (2006) 1868–1878.
- [33] L. Wang, H. Liu, J. Power Sources 134 (2004) 185–196.
- [34] S. Maharudrayya, S. Jayanti, A.P. Deshpande, J. Power Sources 144 (2005) 94–106.
- [35] S. Maharudrayya, S. Jayanti, A.P. Deshpande, J. Power Sources 157 (2006) 358–367.
- [36] W.G. Zhang, P. Hu, X.M. Lai, L.F. Peng, J. Power Sources 194 (2009) 931–940.
- [37] P.K. Jithesh, A.S. Bansode, T. Sundararajan, S.K. Das, Int. J. Hydrogen Energy 37 (2012) 17158–17171.
- [38] K.B.S. Prasad, S. Maharudrayya, S. Jayanti, J. Power Sources 159 (2006) 595–604.
- [39] P.J.S. Vie, S. Kjelstrup, Electrochim. Acta 49 (2004) 1069–1077.